

# Neural network representation of electronic structure from *ab initio* molecular dynamics

Qiangqiang Gu,<sup>1</sup> Linfeng Zhang,<sup>2</sup> and Ji Feng<sup>1,3,\*</sup>

<sup>1</sup>*International Center for Quantum Materials, School of Physics, Peking University, Beijing 100871, China*

<sup>2</sup>*Department of Mathematics and Program in Applied and Computational Mathematics, Princeton University, Princeton, NJ 08544, USA*

<sup>3</sup>*Collaborative Innovation Center of Quantum Matter, Beijing 100871, China*

(Dated: May 23, 2022)

Despite their rich information content, electronic structure data amassed at high volumes in *ab initio* molecular dynamics simulations are generally under-utilized. We introduce a transferable high-fidelity neural network representation of such data in the form of tight-binding Hamiltonians for crystalline materials. This predictive representation of *ab initio* electronic structure, combined with machine-learning boosted molecular dynamics, enables efficient and accurate electronic evolution and sampling. When applied to a one-dimension charge-density wave material, carbyne, we are able to compute the spectral function and optical conductivity in the canonical ensemble. The spectral functions evaluated during soliton-antisoliton pair annihilation process reveal significant renormalization of low-energy edge modes due to retarded electron-lattice coupling beyond the Born-Oppenheimer limit. The availability of an efficient and reusable surrogate model for the electronic structure dynamical system will enable calculating many interesting physical properties, paving way to previously inaccessible or challenging avenues in materials modeling.

## I. INTRODUCTION

Ab initio molecular dynamics (AIMD) is an atomistic simulation method based on *ab initio* electronic structures, and a versatile tool for quantitative understanding thermodynamic and kinetic behaviors of wide range of matter, including molecules, liquids, and solids.[1, 2] In an AIMD simulation, a huge number of atomic configurations have to be sampled for meaningful statistics, during which the Born-Oppenheimer (BO) electronic structure as a function of atomic trajectory is evaluated at *ab initio* level. Although a number of electronic properties can be computed on-the-fly, the electronic structure data, generated at high volumes and significant computation costs, are generally under-utilized, despite exceedingly rich information in these data. This is precisely a situation where a concise and predictive representation of the *ab initio* electronic structure data to harvest the electronic information discarded after AIMD is expected to be highly rewarding. This will constitute a reusable surrogate model, which can significantly expedite the sampling of configuration-dependent electronic structure.

The above problem falls squarely in the realm of deep neural network, which has become a powerful and versatile paradigm for computerized analysis and interpretation of massive data.[3] Through supervised observation of labeled data, a neural network automatically recognizes patterns and regularities in the data and hence becomes predictive regarding the features it is devised to represent. In turn, the predictive neural network can substitute the originally time-consuming calculation

with significant speed-up. For example, Neural network representation of the interatomic potential has been developed and can reproduce the atomic trajectory without time-consuming *ab initio* calculations.[4–8] In these methods, the total potential energy is decomposed into a sum of atomic energy contributions, which is represented by neural networks through the atom and its neighbors (local chemical environment). However, the electronic information available in the AIMD is entirely lost in this approach. Therefore, a predictive representation of electronic structure to pick up the rich electronic structure information in AIMD simulation is highly desirable, which will enable many previous inaccessible or challenging tasks in modeling the electronic properties of a large and dynamical system.

In this paper, we present a neural network architecture to efficiently represent the electronic structure data from AIMD simulations. This architecture will employ a deep feedforward network to process atom trajectory and band structures, to produce a representation that predicts a tight-binding Hamiltonian for a given snapshot of atomic configuration. The main challenge is that the neural network predicted tight-binding (dubbed TBworks hereafter) Hamiltonian is not uniquely determined by its band structure due to the  $U(N)$  gauge freedom, which calls for much effort in designing the neural network architecture and optimization process. It is shown that by the elaborate design of the neural network architecture, the gauge freedom can be reduced. After introducing the architecture and algorithm, the method is tested using a one-dimension charge-density wave (CDW) material, carbyne. It is shown that the *ab initio* electronic structure can be faithfully reproduced by the predicted Hamiltonian. Based on the machine-learned force field, large scale molecular dynamics (MD) simulations are performed on carbyne, during which TBworks can be applied

\* jfeng11@pku.edu.cn

to sample the electronic structures and the derived properties. This enables us to sample the electronic states in the dynamical annihilation of a soliton-antisoliton pair to compute the time-dependent spectral function, beyond the Born-Oppenheimer approximation. Optical conductivity is also obtained by sampling the current-current correlation function in a path-integral molecular dynamics. These results suggest that our TBworks, combined with machine-learned force field, realizes a paradigm for expedited electronic structure sampling at *ab initio* accuracy, which enable capture the non-adiabatic effect in transient processes by large-scale and long-time simulations.

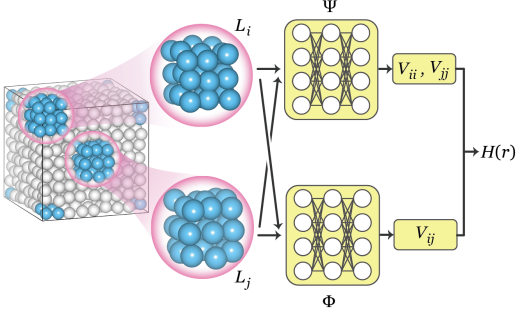


Fig. 1. Schematic of the local chemical environment construction and neural network structure. Ions in local environments  $L_i$  and  $L_j$  are depicted as blue balls enclosed by translucent spheres.  $\Psi$  and  $\Phi$  are multilayer fully connected neural networks with a hyperbolic tangent activation (open circles).

## II. NEURAL NETWORK ARCHITECTURE

In an *ab initio* molecular dynamics simulation, a trajectory of ion positions is generated at a discrete set of time points,  $\mathbf{u}_i(t) = \mathbf{r}_i(t) - \bar{\mathbf{r}}_i$ , where  $\mathbf{r}_i(t)$  and  $\bar{\mathbf{r}}_i$  are respectively the instantaneous and the reference ion positions. Periodic boundary conditions are imposed on the simulation box, such that the *ab initio* eigenstates are Bloch functions. An *ab initio* molecular dynamics yields a set of instantaneous electronic eigenstates for an ionic configuration  $\mathbf{r} = \{\mathbf{r}_i\}$ , with corresponding energy spectrum (bands)  $\hat{\varepsilon}(\mathbf{r}) = \{\hat{\varepsilon}_{n\mathbf{k}}\}$ . The aim is then to use  $\mathbf{r}$  and  $\hat{\varepsilon}(\mathbf{r})$  to train a neural network as a surrogate model for *ab initio* calculation, through a tight-binding electronic Hamiltonian as a function of  $\mathbf{r}$ .

$$H(\mathbf{r}) = \sum_{i \neq j} V_{ij}(\mathbf{r}) c_i^\dagger c_j + \sum_i V_{ii}(\mathbf{r}) c_i^\dagger c_i + \text{H.c.}, \quad (1)$$

where  $V_{ij}(\mathbf{r})$  ( $i \neq j$ ) is a hopping matrix element and  $V_{ii}(\mathbf{r})$  is the on-site energy. Assuming that there is only a single orbital on each ion for notational brevity,  $i$  and  $j$  are also site indices.

Providing the existence of Wannier functions [9–11], it suffices to keep hopping matrix elements between pairs

of orbitals within a finite range. Therefore, We introduce a *local chemical environment* for each site, as shown in Fig. 1. For site  $i$ , the ions lying within a sphere of radius  $R_{\text{cut}}$  centered at  $\mathbf{r}_i$  form its local chemical environment  $L_i = \{j | |\mathbf{r}_j - \mathbf{r}_i| < R_{\text{cut}}\}$ , which assumes non-negligible influence on the Wannier function on site  $i$ . Therefore, the hopping matrix element  $V_{ij}$  will depend on  $\bar{\mathbf{r}}_{ij}$ ,  $\mathbf{u}_i$ ,  $\mathbf{u}_j$ ,  $L_i$ , and  $L_j$ , where  $\bar{\mathbf{r}}_{ij} = \bar{\mathbf{r}}_i - \bar{\mathbf{r}}_j$ . The on-site energy  $V_{ii}$  can be fully determined by  $L_i$ . A naïve neural network for our purpose is composed of two maps (see Fig.1):  $V_{ij} = \Phi(X; \theta)$  and  $V_{ii} = \Psi(Y; \xi)$ , where  $X = (\bar{\mathbf{r}}_{ij}, \mathbf{u}_i, \mathbf{u}_j, L_i, L_j)$ ,  $Y = L_i$ .  $\theta$  and  $\xi$  are trainable parameters of the neural network. The tight-binding Hamiltonian  $H(\bar{\mathbf{r}})$  for reference configuration (usually an equilibrium crystal structure) is easily accessible with standard Wannierization method,[12] which is used to calibrate the neural network in a refined architecture,

$$\begin{aligned} V_{ij} &= \bar{V}_{ij} + \Phi(X; \theta) - \Phi(\bar{X}; \theta), \\ V_{ii} &= \bar{V}_{ii} + \Psi(Y; \xi) - \Psi(\bar{Y}; \xi). \end{aligned} \quad (2)$$

Obviously, when  $\mathbf{r} = \bar{\mathbf{r}}$ ,  $\Phi(X; \theta) - \Phi(\bar{X}; \theta)$  and  $\Psi(Y; \xi) - \Psi(\bar{Y}; \xi)$  equal zero for the neural network to produce exactly  $H(\bar{\mathbf{r}})$ . Although we only show the neural network maps for the cases of single orbital on each ion for brevity, generalization to multi-orbital case is straightforward by allocating individual maps for hoppings between different orbitals.

The maps  $\Phi$  and  $\Psi$  are fulfilled through deep feed-forward neural networks with  $n$  hidden layers neurons, as shown in Fig.1. Take the map  $\Phi$  as an example,  $\Phi = \Phi_n \circ \Phi_{n-1} \circ \dots \circ \Phi_1$ . The  $\mu$ -th hidden layer,  $\Phi_\mu$  takes the output vector of the preceding layer  $x_{\mu-1}$ , and generates a new vector through the component-wise hyperbolic tangent activation,  $x_\mu = \tanh(w_\mu x_{\mu-1} + b_\mu)$ , with  $x_0 = X$ , and  $V_{ij} = x_n$ . Here the matrix  $w_\mu$  reweights  $x_{\mu-1}$  and the vector  $b_\mu$  provides a bias, both of which are adjustable parameters and determined via the Adam stochastic gradient descent method[13] employed to minimize the loss function during a back-propagation process. The loss function is the root-mean-square (rms) deviation between energy spectra  $\varepsilon(\mathbf{r})$  computed from predicted  $H(\mathbf{r})$  and training labels from the *ab initio*  $\hat{\varepsilon}(\mathbf{r})$ . In principle,  $H(\mathbf{r})$  is not uniquely determined by energy spectra  $\hat{\varepsilon}(\mathbf{r})$  alone due to the existence of gauge freedom. If a different gauge is chosen at different  $\mathbf{r}$ ,  $H(\mathbf{r})$  as a function of  $\mathbf{r}$  may not necessarily be smooth and continuous. Because of the discontinuity, the predicted  $H(\mathbf{r})$  may not interpolate well for unseen configurations, not to mention extrapolations. Fortunately, the continuity of  $H(\mathbf{r})$  is fulfilled automatically in our neural network implementation, since the relationships between  $\mathbf{r}$  and  $H(\mathbf{r})$  are represented by  $\Phi$  and  $\Psi$ , which are smooth and continuous composite maps. Indeed, the TBworks gives the desired performance in the test example to be discussed next.

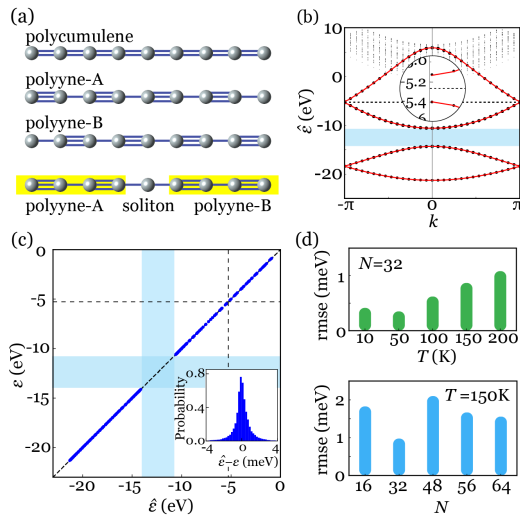


Fig. 2. Performance of neural network representation of the electronic structure of carbyne. (a) Structure of carbyne, including (from top to bottom) polycumulene, two polyynes, and a chain with a kink excitation. (b) TBworks (red line) and *ab initio* (black dots) band structure for polyynes. Blue shaded region indicates the  $s$ - $p$  separation, and the black dashed line indicates the CDW gap (a blow-up view in the inset). (c) TBworks predicted vs *ab initio* eigenvalues for unseen snapshots with different simulation box sizes and temperatures,  $T = 10, 50, 100, 150, 200$  K and  $N = 16, 32, 48, 56, 64$ . Inset: error distribution. (d) Generalization root-mean-square error (rmse) for unseen snapshots with a simulation box size  $N = 32$  at different temperatures (upper panel) and snapshots at  $T = 150$  K with different simulation box sizes (lower panel).

### III. ACCURACY AND TRANSFERABILITY

We now proceed to evaluate the performance of our neural network algorithm by learning and then predicting AIMD eigenvalues for a charge-density wave material, carbyne.[14–16] Carbyne is a one-dimensional  $sp^1$  hybridized carbon chain, which can undergo an archetypal Peierls’ transition[17] from polycumulene ( $=C=C=$ ) to polyynes ( $-C\equiv C-$ ). Polyynes has two degenerate ground state structures interrelated by a shift of the single and triple bonds, as shown in Fig.2(a). Polyynes can be characterized by the order parameter  $u_\alpha = (-1)^\alpha u_0$  ( $\alpha = 1, 2, \dots, N$ ), and  $\text{sign}(u_0) = \pm 1$  corresponds to the two degenerate phases. Remarkably,  $\text{sign}(u_0) = \pm 1$  can coexist on a single carbyne chain, separated by a domain wall or a kink in  $u_\alpha$ , which can lead to solitonic excitations.[18] Bond ordering and solitonic excitations make carbyne an interesting and non-trivial material for testing our algorithm.

The *ab initio* molecular dynamics in carbyne with the canonical ensemble are performed by the Vienna *ab initio* simulation package with the generalized-gradient approximation[19, 20] to generate the training data for TBworks. Nose-Hoover thermostat[21, 22] is used to

maintain the temperatures. The cutoff energy is 400 eV for wave functions expansion in the plane-wave basis sets. The AIMD simulations are performed with the simulation box sizes containing  $N = 16, 32, 48, 56$  and 64 carbon atoms and at temperatures  $T = 10, 50, 100, 150$ , and 200 K. The eigenvalue labels are calculated using  $1 \times 1 \times 4$  and  $1 \times 1 \times 2$   $k$ -mesh for  $N = 16$  and  $N = 32$  boxes, while for  $N > 32$ , only the  $\Gamma$  point is used. In order to train the TBworks, labeled data from 5000 AIMD snapshots within one the trajectory with  $N = 32$  at  $T = 150$  K. The generalizability and transferability of TBworks are validated against multiple unlearned data sets (5000 AIMD snapshots each) from multiple  $T$  and  $N$ .

In carbyne, the C-C  $\sigma$  bonds are formed by the overlap of  $sp^1$  hybridized orbitals while the  $\pi$  bonds are formed by the other two half-filled  $p$  orbitals perpendicular to the carbon chain. The  $s$  and  $p$  bands within the energy window ( $-22 - 0$  eV) are picked out as label data from 5000 AIMD snapshots of  $N = 32$  C atoms at  $T = 150$  K to train the TBworks. Fig.2(b) displays a faithful reproduction of the band structure of polyynes by the trained TBworks, including the charge-density wave gap  $\Delta \sim 27$  meV. The reproduction of band structures for more structures can be seen in the Fig.S1 in supplementary materials.[23] In Fig.2(c), the TBworks predicted spectra for snapshots unseen in training are plotted against *ab initio* spectra, where samples are drawn from AIMD with multiple temperatures (10 – 200 K) and a range of simulation box sizes. The generalization error (rms deviation) of these predictions is  $\sim 1$  meV and the coefficient of determination  $R^2 = 0.99999994$ . The  $s$ - $p$  separation of  $\sim 3.72$  eV and the CDW gap  $\sim 27$  meV are also well reproduced despite their disparate energy scales. As is also shown in Fig.2(d), the generalization error of the TBworks trained at a single  $T$  and  $N$  are on the order of 1 meV, when tested against data from multiple temperatures and simulation box sizes. Therefore, we conclude that the TBworks trained at a single  $T$  and  $N$  offers a faithful representation of the *ab initio* electronic structure, which is also highly transferable to a range of temperatures and system sizes unseen in the initial learning.

With the accuracy perfectly preserved, we further investigate the efficiency of the TBworks model. As shown in Fig.3, due to the inevitable diagonalization procedure, the computation cost of both the TBworks and *ab initio* calculations scale roughly as  $\sim N^3$ , where  $N$  denotes the system size. However, the prefactor is different by more than 5 orders of magnitude. This is because in *ab initio* calculations, diagonalization happens in solving the Kohn-Sham equations[24], where the one-electron wavefunctions are expanded over a large basis set of size proportional to but way larger than  $N$ ; while in TBworks, the size of the Hamiltonian is the number of Wannier orbitals, which is generally of the same order of  $N$ . As such, the dramatic speed-up in TBworks makes the accessible system size around 2 orders of magnitude larger than *ab initio* calculations.

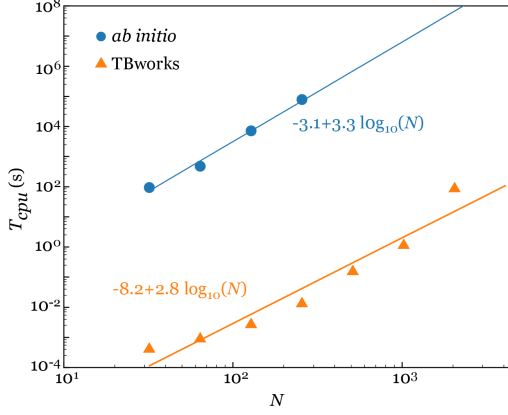


Fig. 3. Compute time  $T_{cpu}$  for calculating the electronic spectra of carbyne vs system size  $N$  in *ab initio* and TBworks calculations. Here  $T_{cpu}$  is the CPU time on a compute node equipped with 2 AMD EPYC-7452 CPUs (64 cores). The *ab initio* calculation is performed at  $\Gamma$  point[19], with plane-wave basis cutoff at 400 eV and total energy convergence to within  $10^{-4}$  eV per atom. The dots (*ab initio*) and triangles (TBworks) mark the computation costs for different  $N$ . The solid lines are the least-square linear fittings between variable  $\log_{10}(T_{cpu})$  and  $\log_{10}(N)$ .

Further insights into the performance of the TBworks are gained by visualizing the training process on a reduced information plane.[25, 26] The mutual information  $I(a; b)$  is an asymmetric measure of the correlation between a pair of random variables  $a$  and  $b$ , with distributions  $P(a)$  and  $P(b)$ , respectively,

$$I(a; b) = D_{KL}(P(a, b) || P(a) \otimes P(b)) \quad (3)$$

where  $D_{KL}$  is the Kullback-Leibler divergence and  $P(a, b)$  is the joint distribution.[27] We compute the mutual information between the input  $x$  (ionic coordinates inside a simulation box) and the output of the  $n$ -th layer  $y_n$ , and the mutual information between the training label  $\hat{\epsilon}$  and the output  $y_n$ . Thus we can visualize the evolution of the neural network on the reduced information plane  $I(x, y_n) - I(\hat{\epsilon}, y_n)$ , as depicted in Fig.4. We see that  $I(\hat{\epsilon}, y_1)$  undergoes a continuous sharp increase throughout the training, which directly results from the optimization of the loss function, indicating continued improvement of model fitting.  $I(x, y_1)$  increases slightly then decreases in the later stage. The decrease in  $I(x, y_1)$  is a manifestation of reduction of data redundancy, which is very important for the performance of the neural network. The dynamics of layers 2 and 3 are also bi-phasic, where redundancy elimination precedes the rapid model improvement. The redundant information on  $x$  arises from a large cut-off radius  $R_{cut}$  for the local chemical environment, which includes atoms having little impact on the hopping amplitude. Therefore, the information plane analysis uncovers critical stages in the learning process of neural network during the training process, and offers

leads for systematically optimizing the choice of setup parameter for TBworks.

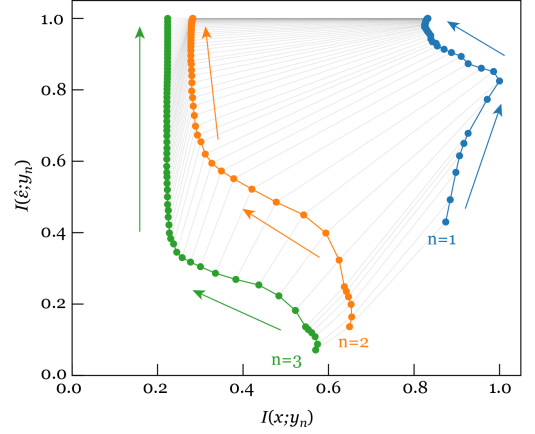


Fig. 4. Information plane loci of a 3-layer TBworks during training, showing the mutual information trajectories of a [200, 200, 200] neural network in 800 epoches. The colored solid arrows are guide-of-eye indications of the direction of progression for the three loci.

#### IV. APPLICATIONS TO KINETIC AND EQUILIBRIUM SAMPLING

The efficient, accurate and transferable access to  $H(\mathbf{r})$  offered by our TBworks provides a convenient computational tool for investigating the correlation between electronic and ionic degrees of freedom, which is particularly important for systems with strong electron-phonon coupling. In this section, TBworks is employed to evaluate correlation functions and corresponding physical properties of dynamical (both transient and equilibrium) systems. In the first example we compute the time-dependent spectral function of a kinetic process of soliton annihilation, whereupon non-adiabatic effects are revealed. As a second example, it is demonstrated TBworks can be combined with path-integral molecular dynamics to compute the current-current correlation function and therefore the optical conductivity.

The soliton-antisoliton pair annihilation process is one such example, where the zero-energy electronic modes are gapped out dynamically. Non-adiabatic effect can be important but difficult to study in AIMD due to the high demand for computational resources. In order to study this kind of process, we interface our TBworks with the machine-learned force field[8] to perform highly efficient classical molecular dynamics (CMD) and path-integral molecular dynamics (PIMD) on carbyne by the LAMMPS[28]. The machine-learned force field is generated by DeePMD-kit[29] using a  $200 \times 200 \times 200$  deep neural network trained by 10000 snapshots of labeled AIMD data and tested by a validation set containing 1000 snapshots. The rms error is found to be within 0.01 eV/Å for



predicted forces, and  $10^{-5}$  eV per atom for predicted energies, which means the accuracy of the machine-learned force field is at the same level of the ab initio calculation. Both the classical and path-integral MD simulations are performed in the canonical ensemble on a supercell containing 1024 C atoms with a time step of 0.2 femtoseconds (fs) at different temperatures. The Nose-Hoover thermostat[21, 22, 30] is employed to control the temperatures in the canonical ensemble. In PIMD, the paths are discretized into 12 imaginary time slices. Fig.5(a) shows the order parameters  $u_\alpha$  of the ionic configurations in the dynamical process where soliton-antisoliton pair is annihilated from the classical MD trajectory initialized with soliton structure at  $T = 1$  K.

To highlight the non-adiabatic dynamical effect in the soliton-antisoliton pair annihilation, we take a close look at the time-dependent electronic spectral functions. Because of the quick access to TBworks Hamiltonian, we are able to let the electronic system evolve according to  $\mathcal{T}e^{-i \int_{t_0}^t H(r(t'))dt'}$  ( $\hbar = 1$ ). Doing so explicitly takes ion dynamics into account and is manifestly beyond the BO approximation. As ion dynamics breaks time homogeneity for electrons, we define a time-dependent spectral function as

$$A(\omega, t) = \frac{i}{2\pi N} \hat{F} \text{Tr} [G^R(t + \tau, t) - G^A(t + \tau, t)] \quad (4)$$

where  $G_{\alpha\beta}^{A/R}(t + \tau, t) = \pm i \theta(\mp \tau) \langle \{c_\alpha(t + \tau), c_\beta^\dagger(t)\} \rangle$  are advanced/retarded Green's functions, and  $\hat{F}$  means a Fourier transform w.r.t. the time difference  $\tau$ . [31] At different  $t$ , the advanced and retarded Green's functions are evaluated by computing the expectation of the commutator  $\{c_\alpha(t + \tau), c_\beta^\dagger(t)\}$  for  $\tau > 0$  and  $\tau < 0$ , respectively, with  $|\tau| \leq 600$  for an energy resolution of  $\sim 3$  meV ( $\sim 10\%$  of the CDW gap). As the exact propagator from the TBworks Hamiltonian can be quickly computed, the  $A(\omega, t)$  so obtained can be non-adiabatically calculated along a trajectory in the MD simulation. As a comparison, the static electronic spectral function within the BO approximation for configuration at  $t$  is calculated using instantaneous energy spectra, with  $A_{\text{stat}}(\omega, t) = \frac{1}{N_k} \sum_{nk} \delta(\omega - \varepsilon_{nk}(t))$ .

We focus on the soliton-antisoliton pair annihilation event indicated by the dashed rectangle in Fig.5(a). During this event, two kinks meet and annihilate, and the polyne-B phase completely disappears. At the same time, the degenerate zero-energy modes localized at the kinks become hybridized and a gap gradually develops. The question is whether the BO approximation is accurate enough to describe the electronic states for the dynamical annihilation process. As a comparison, we firstly examined the electronic spectral functions for structures well before (Fig.5(c)) and after (Fig.5(d)) the annihilation event. Prior to the annihilation event where the soliton and anti-soliton are well separated, both dynamical (beyond BO approximation) and static (within BO approximation) spectral functions give the same topolog-

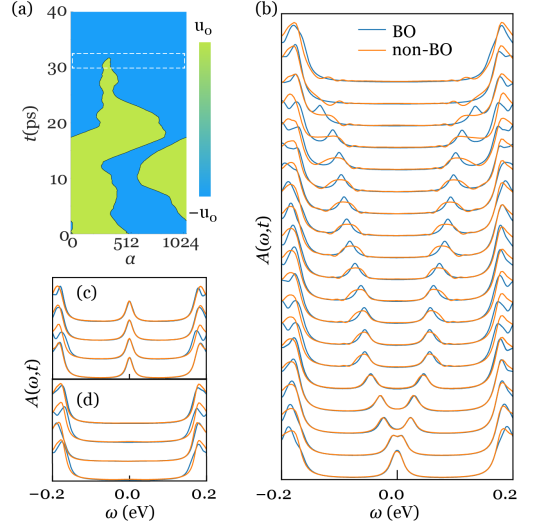


Fig. 5. Non-adiabatic dynamical effect on the electronic spectral functions during the soliton-antisoliton pair annihilation process. (a) The order parameter along a polyne chain as a function of time in a molecular dynamics trajectory. The dashed rectangle indicated the soliton-antisoliton pair annihilation event. (b) Computed time-dependent electronic spectral functions for structures at every 20 fs in the annihilation event. (c)(d) Computed electronic spectral functions for structures before (c) and after (d) annihilation event.

ical protected zero-energy peaks, as shown in Fig.5(c), where little difference between the dynamical and static spectral functions is discernible. Post annihilation, the carbyne chain adopts a homogeneous polyne-A structure, where both dynamical and static spectral functions present the CDW gap, as shown in Fig.5(d). Again, little difference between the dynamical and static spectral functions is uncovered, because the system is in a (transient) stationary state. For the case during this annihilation event, the dynamical and static time-dependent spectral functions for the annihilation process are calculated and shown in Fig.5(b). Both dynamical and static spectral functions show the splitting of the zero-energy modes into two peaks, which subsequently merge into the conduction and valence bands respectively as the soliton-antisoliton pair approaching to annihilation. The difference is that the energy peaks in the dynamical spectral functions show a larger broadening than those in the static spectral functions. In short, although the dynamical effect shows little renormalization on the spectral functions before and after the annihilation event, as far as the pair annihilation process is concerned, the non-adiabatic dynamical effect is prominently visible in our calculations.

Now we move on to examine some of the equilibrium electronic correlation function based on TBworks, again with carbyne as the model material, using classical and path-integral molecular dynamics. In order to compute experimentally accessible electronic properties, retarded

correlation functions of the form

$$G_{AB}^R(t-t') = -i\lambda\Theta(t)\text{Tr}\{\varrho_{\text{ion}}(\mathbf{r}')\langle[A(t),B(t')]_s\rangle\} \quad (5)$$

usually need to be computed, where  $s = \pm$  for Fermion/Boson and  $\lambda$  is a numerical constant. In an equilibrium ensemble, the sampling according to ionic density matrix  $\varrho_{\text{ion}}(\mathbf{r}(t'))$  is automatically offered by the trajectory from molecular dynamics. Anticipating little nonadiabatic effects, we use the approximate propagators:  $U(t-t') \approx e^{-iH(t')(t-t')}$ . Then the electronic spectral function is computed with  $A \rightarrow \hat{\psi}, B \rightarrow \hat{\psi}^\dagger$  and  $\lambda = i/2\pi N$ . To compute the electronic conductivity,  $A, B \rightarrow j = -env$  the current operator. Then the dissipative part of the conductivity is given by

$$\text{Re}\sigma(\omega) = \text{Re}\left[\frac{i}{\omega}\hat{F}G_{jj}^R(t)\right]. \quad (6)$$

For the Fourier transformation, time values  $t-t' \in [-600, 600]$  fs are used with 0.1 fs increment. Further details of the calculation of these correlation functions can be found in Supplementary Materials.[23]

The spectral function and optical conductivity for carbyne at finite temperatures are shown in Fig. 6. We can see that at  $T = 1$  K, the spectral functions from both path-integral and classical simulations show a CDW gap  $\Delta \sim 27$  meV, indicating the equilibrium configuration of carbyne is in the polyne structure. The optical conductivity also shows an onset at  $\omega = \Delta$  at this temperature. At  $T = 10$  K, the spectral function remains gapped in CMD, indicating absence of soliton. In contrast, PIMD shows a zero energy peak in spectral function, which suggests quantum effect promotes the generation of soliton-antisoliton pairs. As shown in Fig.S2 in the supplementary materials,[23] the energy barrier for generation of a soliton-antisoliton pair from the polyne structure is  $\sim 80$  meV. Therefore, at low temperature 10 K, the soliton-antisoliton pair is hardly sampled in CMD. However, in PIMD due to quantum dynamical effect, the creation of soliton-antisoliton pair can be observed.

When the temperature is raised to moderately high value 100 K, in PIMD, the CDW gap and the zero energy mode disappear and optical conductivity shows the single peak at  $\omega = 0$ , which is commensurate with the polycumulene phase. At the same temperature in CMD, the zero energy peak in spectral function indicates presence of solitons. Above 300 K, in the classical molecular dynamics, CDW melts and polycumulene is the equilibrium structure. Both spectral function and optical conductivity present the sequence of phase transition in carbyne from polyne to soliton and finally polycumulene in CMD and PIMD sampling. Due to the quantum dynamical effect, the soliton and polycumulene phase transitions happen at lower temperatures in PIMD than that in CMD, which could be detected by measuring the spectral function and/or optical conductivity experimentally.

All these results exhibit the efficiency of our TBworks in calculating correlation functions that can be routinely measured in experiment to monitor the dynamics and phase transition but require large scale and long time simulations.

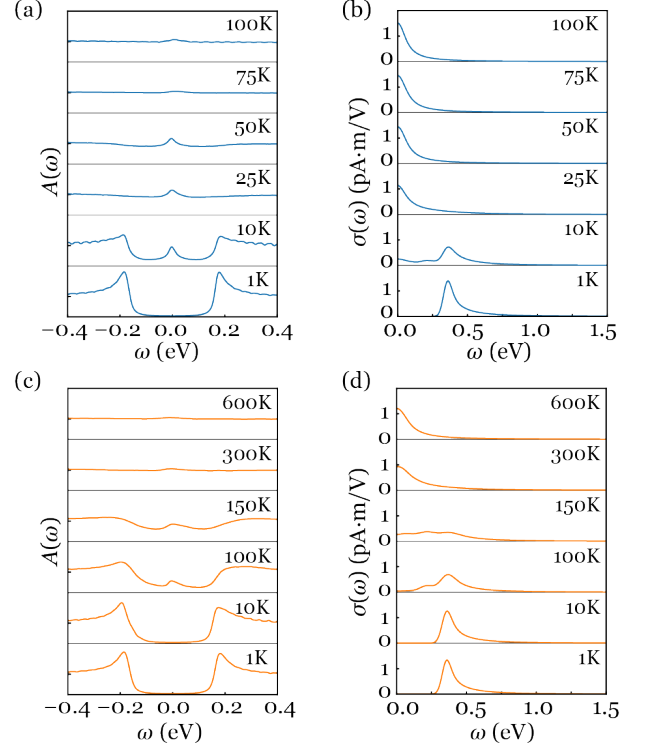


Fig. 6. The averaged electronic spectral function  $A(\omega)$  and optical conductivity  $\sigma(\omega)$  for supercell  $N = 1024$  at different temperatures. Spectral function (a)(c) and optical conductivity (b)(d) averaged in the canonical ensemble sampled by PIMD (blue lines) and CMD (orange lines).

## V. SUMMARY

In this work, we have developed a neural network-based predictive representation method, which predicts tight-binding Hamiltonians for modeling electronic structures. This method provides an efficient approach to configuration-dependent Hamiltonians by directly supervised observation of the *ab initio* energy spectra. This enables an expedited access to electronic structures at dramatically reduced computational costs during the atomic configurations sampling, in subsequent molecular dynamics or Monte Carlo. Considering the example of carbyne, we demonstrate the accuracy of our method in predicting the electronic spectra is comparable to that of the *ab initio* calculations. The TBworks also shows a high degree of transferability, accurately predicting spectra for configurations drawn from unseen temperatures and system sizes.

By interfacing our TBworks with a machined-learned

force field it is demonstrated that we can efficiently sample the electronic structure of carbyne in molecular dynamics to compute correlation functions. This enables the computation of Green's functions and the time-dependent spectral functions in the dynamical annihilation of a soliton-antisoliton pair. When compare our results with those from the adiabatic approximation, it is found that the low-energy edge modes is significant renormalized due to the non-adiabatic dynamical effect. We have also applied the TBworks sampling of electronic structure in a path-integral molecular dynamics, where the optical conductivity is computed by sampling the current-current correlation function.

These results suggest that the TBworks approach provides an efficient and accurate computation tool for sampling electronic structure in order to compute correlation functions and associated physical properties. The low computational cost, accurate and transferable electronic model and dramatic speed-up of a combined machine-learned force field and TBworks for such purposes as compared shall enable large-scale and long-time simulation,

and as we have demonstrated, capturing non-adiabatic effect in transient processes. Therefore, this approach will significantly enhance our capability and broaden the scope in the modeling of electronic structure and processes in materials at finite temperatures or in kinetic phenomena.

## ACKNOWLEDGMENTS

This work is supported by the National Natural Science Foundation of China (Grant No. 11725415 and No. 11934001), the Ministry of Science and Technology of China (Grant No. 2018YFA0305601 and No. 2016YFA0301004), and by the Strategic Priority Research Program of Chinese Academy of Science (Grant No. XDB28000000). One of the authors (L.Z.) has been supported in part by the Center for Chemistry in Solution and at Interfaces (CSI), Princeton, funded by the DOE Award DE-SC0019394.

- 
- [1] R. Car and M. Parrinello, *Phys. Rev. Lett.* **55**, 2471 (1985).
  - [2] D. Marx and J. Hutter, *Ab Initio Molecular Dynamics: Basic Theory and Advanced Methods* (Cambridge Univ. Press, 2009).
  - [3] Y. LeCun, Y. Bengio, and G. Hinton, *Nature* **521**, 436 (2015).
  - [4] J. Behler and M. Parrinello, *Phys. Rev. Lett.* **98**, 146401 (2007).
  - [5] K. T. Schütt, F. Arbabzadah, S. Chmiela, K. R. Müller, and A. Tkatchenko, *Nat. Commun.* **8**, 13890 (2017).
  - [6] J. S. Smith, O. Isayev, and A. E. Roitberg, *Chem. Sci.* **8**, 3192 (2017).
  - [7] L. Zhang, J. Han, H. Wang, R. Car, and W. E, *Phys. Rev. Lett.* **120**, 143001 (2018).
  - [8] L. Zhang, J. Han, H. Wang, W. Saidi, R. Car, and W. E, *Adv. Neural Inf. Process. Syst.* **32**, 4436 (2018).
  - [9] C. Brouder, G. Panati, M. Calandra, C. Mourougane, and N. Marzari, *Phys. Rev. Lett.* **98**, 046402 (2007).
  - [10] J. D. Cloizeaux, *Phys. Rev.* **135**, A698 (1964).
  - [11] G. Nenciu, *Comm. Math. Phys.* **91**, 81 (1983).
  - [12] N. Marzari, A. A. Mostofi, J. R. Yates, I. Souza, and D. Vanderbilt, *Rev. Mod. Phys.* **84**, 1419 (2012).
  - [13] D. P. Kingma and J. Ba, *arXiv preprint arXiv:1412.6980* (2014).
  - [14] R. B. Heimann, J. Kleiman, and N. M. Salansky, *Nature* **306**, 164 (1983).
  - [15] C. Jin, H. Lan, L. Peng, K. Suenaga, and S. Iijima, *Phys. Rev. Lett.* **102**, 205501 (2009).
  - [16] O. Cretu, A. R. Botello-Mendez, I. Janowska, C. Pham-Huu, J.-C. Charlier, and F. Banhart, *Nano Lett.* **13**, 3487 (2013).
  - [17] M. Kertesz, J. Koller, and A. Azman, *J. Chem. Phys.* **68**, 2779 (1978).
  - [18] W. P. Su, J. R. Schrieffer, and A. J. Heeger, *Phys. Rev. Lett.* **42**, 1698 (1979).
  - [19] G. Kresse and J. Furthmüller, *Phys. Rev. B* **54**, 11169 (1996).
  - [20] J. P. Perdew and A. Zunger, *Phys. Rev. B* **23**, 5048 (1981).
  - [21] S. Nosé, *Mol. Phys.* **52**, 255 (1984).
  - [22] W. G. Hoover, *Phys. Rev. A* **31**, 1695 (1985).
  - [23] Supplementary Materials.
  - [24] W. Kohn and L. J. Sham, *Phys. Rev.* **140**, A1133 (1965).
  - [25] N. Tishby and N. Zaslavsky, in *2015 IEEE Information Theory Workshop (ITW)* (2015) pp. 1–5.
  - [26] R. Shwartz-Ziv and N. Tishby, *arXiv preprint arXiv:1703.00810* (2017).
  - [27] S. Kullback and R. A. Leibler, *Ann. Math. Statist.* **22**, 79 (1951).
  - [28] S. Plimpton, *J. Comput. Phys.* **117**, 1 (1995).
  - [29] H. Wang, L. Zhang, J. Han, and W. E, *Comput. Phys. Commun.* **228**, 178 (2018).
  - [30] M. E. Tuckerman, B. J. Berne, G. J. Martyna, and M. L. Klein, *J. Chem. Phys.* **99**, 2796 (1993).
  - [31] H. T. M. Nghiem and T. A. Costi, *Phys. Rev. Lett.* **119**, 156601 (2017).